International Journal of Heat and Mass Transfer 52 (2009) 3525–3533

Contents lists available at ScienceDirect

International Journal of Heat and Mass Transfer

journal homepage: www.elsevier.com/locate/ijhmt

Numerical analysis for a vapor feed miniature direct methanol fuel cell system

Bin Xiao, Amir Faghri *

Department of Mechanical Engineering, University of Connecticut, 261 Glenbrook Road, Unit 2337, Storrs, CT 06169, United States

ARTICLE INFO

Article history:
Received 2 February 2009
Received in revised form 7 March 2009
Accepted 7 March 2009
Available online 17 April 2009

Keywords:
Direct methanol fuel cell
Vapor feed
Model

ABSTRACT

A two-dimensional, multiphase model is presented and analyzed for a vapor feed DMFC system. The DMFC model is based on the multiphase mixture formulation and encompasses all components in the porous regions of a vapor feed DMFC using a single computation domain. The evaporation/condensation phenomenon in the anode flow channel is modeled in a separated way. An iterative numerical scheme is used to solve the governing equations in a coupled manner. Numerical simulations are carried out to explore the transient and polarization characteristics of the DMFC, including methanol crossover through the membrane, temperature evolution, anodic and cathodic overpotentials. The results indicate the anode flow channel for the feeding methanol solution is the key parameter for the DMFC performance. The numerical results are also compared with the experimental data with good agreement.

1. Introduction

Direct methanol fuel cell (DMFC) is a further development of familiar hydrogen polymer electrolyte membrane fuel cell (PEMFC) technology. It uses methanol in the form of vapor or liquid to generate electrical energy under relatively low temperature (<100 °C) [1–3]. The structure of a DMFC consists of two gas diffusion layers and two porous electro-catalytically active electrodes on either side of a solid polymer electrolyte (SPE) membrane. DMFC is considered as a promising portable power source with the advantages including high efficiency, very low emissions and fast refueling, but still has to overcome challenges with respect to efficiency and power density [4–6]. DMFCs have a low output voltage and the main losses are essentially associated with poor electro-activity on the anodic oxidation of methanol. In addition to this difficulty, the DMFC has serious methanol permeation through the polymer membrane, which reduces results in mixed potential formation at the cathode and reduces the energy yield of the cell and methanol efficiency.

Compared with a liquid feed system, although a vapor feed system has longer start-up since fuel pre-heating is necessary before injection, it offers higher reaction activities because of the usage of highly concentrated fuel and higher temperature. On the other hand, the methanol crossover in the vapor feed DMFC is much lower than the liquid feed DMFC. In the vapor feed DMFC, methanol evaporates from a nearly pure liquid methanol source and condenses into a highly dilute methanol solution at the anode side of a fuel cell. In order to eliminate the external components such as pumps and compressors, the air and liquid methanol can be delivered in the passive ways by the forces of natural convection and capillary forces.

During the past decade, significant efforts have been directed toward the creation of low cost and effective DMFC. Kim [7] designed a vapor feed passive DMFC in which the vapor is transported through a vaporizer, barrier and buffer layer. The results showed that the vapor feed passive DMFC with humidified MEA maintained 20–25 mW/cm^2 power density for 360 h and performed with a 70% higher fuel efficiency, and 1.5 times higher energy density than those in a liquid feed passive DMFC. Guo and Faghri [8] provided vapor feed DMFCs with passive thermal/fluids management systems. Pure methanol was delivered by the wick structures from a liquid methanol reservoir to an evaporation pad, where the liquid was evaporated by different heating manners such as electrical heating, catalyst burning and heat recovery from the cell itself. The results showed that the vapor feed DMFC reached a power density of 16.5 mW/cm^2 at a current density of 60 mA/cm^2. The results demonstrated long-term operation, easy fuel delivery control and scalability to larger power systems. A two-cell stack has successfully operated 6 months with negligible degradation. Based on the above vapor feed DMFC system, Jewett et al. [9] developed a vapor feed passive DMFC system with the additional buffer layer at the inlet of the anode to promote water and methanol distribution as well as mixing of the fluids. The results showed a maximum power density of 33 mW/cm^2 and 120 h of continuous operation at a constant current of 50 mA/cm^2. The fuel utilization efficiency during the performance was 34.8% and the energy efficiency was 8.2%.

As numerical models of the vapor feed DMFC can reveal the physicochemical mechanisms and provide a useful tool for the optimization of cell design and operating conditions, the vapor feed DMFC modeling has been developed to analyze the

* Corresponding author. Tel.: +1 860 486 0419; fax: +1 860 486 0479.
E-mail address: faghri@engr.uconn.edu (A. Faghri).

0017-9310/$ - see front matter © 2009 Elsevier Ltd. All rights reserved.
doi:10.1016/j.ijheatmasstransfer.2009.03.009

Nomenclature

A	area of fuel cell (m^2)
a	constant in coefficient matrix
a_{ox}	specific area for oxidation (m^{-1})
a_{red}	specific area for reduction (m^{-1})
b	element in solution matrix
$\mathbf{B}$	coefficient matrix for Stefan–Maxwell (s/m^2)
c_{MeOH}	methanol concentration in liquid (mol/cm^3)
c_{H_2O}	water concentration in liquid (mol/cm^3)
d_g	characteristic length of gas phase (m)
D_{ij}	binary diffusivity (m^2/s)
$D_{eff,ij}$	effective diffusivity of gas phase (m^2/s)
F	Faraday constant (C/mol)
h_{fg}	latent heat of vaporization (J/kg)
h_m	mass transfer coefficient (m s)
$I_{0,ref}^{MeOH}$	oxidation exchange current density (A/m^2)
$I_{0,ref}^{O_2}$	reduction exchange current density (A/m^2)
$\mathbf{I}$	current density (A/m^2)
$\mathbf{I}_p$	proton current density ($proton/m^2$ s)
$\mathbf{J}$	mass flux (kg/m^2 s)
$J(s)$	Leverette function
k_{rg}	relative permeability of gas phase
k_{rl}	relative permeability of liquid phase
$\mathbf{K}$	permeability (m^{-2})
$\dot{m}'''$	mass source (kg/m^3 s)
M_i	molecular weight of component i (kg/mol)
M_g	molecular weight of gas (kg/mol)
M_l	molecular weight of liquid (kg/mol)
$\mathbf{n}$	surface normal vector
n_d	electro-osmotic drag coefficient (mol/mol)
p_c	capillary pressure (Pa)
p_l	liquid pressure (Pa)
p_g	gas pressure (Pa)
R_u	ideal gas constant (J/mol K)
R_Ω	resistance (Ω)
R_{ox}	oxidation reaction rate (A/m^3)
R_{red}	reduction reaction rate (A/m^3)
Re_ε	pore Reynolds number
t	time (s)
T	temperature (K)
s	liquid saturation
$\mathbf{V}_k$	velocity of phase k (m/s)
$\langle \mathbf{V}_k \rangle^k$	intrinsic phase velocity of phase k (m/s)
V	volume (m^3)
x_{MeOH}	mole fraction of methanol in liquid (mol/mol)
x	distance in x-direction (m)
y	distance in y-direction (m)

Greeks

α_l	liquid volume fraction
$\alpha_{l,MeOH}$	volume fraction of MeOH in liquid phase
α_a	anode transfer coefficient
α_c	cathode transfer coefficient
ε	porosity
η	fuel consumption efficiency
η_a	anodic overpotential (V)
η_c	cathodic overpotential (V)
λ	oxidation constant (mol/cm^3)
μ	viscosity (N s/m^2)
θ	contact angle between liquid and solid (rad.)
σ	surface tension (N/m)
σ_c	electrical conductivity of carbon phase (Ω^{-1} m^{-1})
σ_m	proton conductivity of membrane phase (Ω^{-1} m^{-1})
ρ	density (kg/m^3)
τ	tortuosity
$\omega_{g,i}$	mass fraction of gas (kg/kg)
$\omega_{l,i}$	mass fraction of liquid (kg/kg)

Subscripts

acl	anode catalyst layer
$agdl$	anode gas diffusion layer
ccl	cathode catalyst layer
$cgdl$	cathode gas diffusion layer
e	entrance
g	gas
i	component i
j	component j
l	liquid
m	membrane
n	neighboring cells
R	due to chemical reaction
T	due to mass transport (evaporation/condensation)

Superscripts

k	previous iteration
$k+1$	next iteration

performance of DMFC in a different prospective in past years. Few models for the vapor feed DMFC have been developed in past years. Scott et al. [4] were first to introduce a semi-empirical model to simulate the performance of their vapor-feed DMFC. The model considered methanol crossover across the polymeric membrane owing to diffusion, osmotic drag, and convection assuming a linear change in methanol concentration across the membrane. Also, the model assumed the methanol crossover potential to be a linear function of methanol crossover flux. The overpotential caused by methanol crossover was assumed to be proportional to the concentration of methanol at the cathode and the membrane was considered fully hydrated. Transport along the flow channel was described by plug flow and the transport in the electrodes was not considered in their model.

Dohle et al. [10] presented an isothermal, steady state, one-dimensional model for the vapor-feed DMFC, and the crossover phenomenon was described. The numerical calculation was based on the finite integration technique and was performed on the mathematical and physicochemical basis of an earlier-developed PEMFC model. The diffusion in the transition region is assumed by a superposition of Knudsen diffusion and Stefan–Maxwell diffusion. The physical properties of the membrane related to water content were taken into account in the model. The interdependence of the respective partial pressure and the liquid concentration in the membrane phase was described by Henry's law. The effects of methanol concentration on the cell performance were studied. A two-dimensional macro-homogeneous model to describe the reaction and transport for vapor-feed configurations, has been presented by Kulikovsky et al. [11], employing Stefan–Maxwell molecular diffusion primarily in the gas diffusion layers and the Knudsen diffusion mechanism mainly in the catalyst layers, while neglecting the methanol crossover and the influence of the normal gradients in the flow channel. Recently, Rice and Faghri [12] developed a one dimensional analysis of the transport phenomena of a vapor feed DMFC system. The net water produced was found to be greater than the water evaporated for several different vapor diffusion lengths.

Although the fuel delivery to the fuel cell is an important factor for the success of the vapor feed DMFC systems, none of the above models considered the evolution of fuel transport in the flow chan-

nel as well as the transient hydrodynamic behavior in the vapor feed DMFC. The objective of this study is to present a two dimensional, transient, multiphase model for a vapor feed DMFC. The model focuses on three important requisites: (i) the transient transport phenomena and fuel cell performance, (ii) the treatment of polarization effects on the performance of the DMFC, and (iii) an appropriate description of methanol and water condensation/evaporation phenomena in the flow channel. Although the present results are specific to a specific single cell, the model is in all other respects generic as it provides the essential information on the interactive nature of the various electrochemical, physical and chemical processes taking place in the DMFC system. Thus, the model can provide feedback on specific modifications that can be made before the finalizing of the vapor methanol delivery and fuel cell design that would potentially improve the achieved power output.

2. Mathematical model

The main transport phenomenon in the vapor-feed DMFC is methanol evaporating from a nearly pure liquid methanol source and condensing into a highly dilute methanol solution at the anode side of a fuel cell. As the methanol solution flows down, the mass fraction of the methanol decreases along the fuel cell due to the electrochemical reactions in the electrodes and evaporations in the fuel cell layers.

The typical schematic of a vapor feed DMFC delivery system and the membrane exchange assembly is illustrated in Fig. 1. The operating mechanisms for a DMFC are typically characterized by the transport of liquid–gas mixture and protons, and the transformation of species by electrochemical reactions. Gaseous methanol evaporated by an external heater enters the anode flow channel, is condensed in the liquid pad which is connected with the porous gas diffusion layer, and then reaches the catalyst layer. The methanol then dissociates to protons and electrons within the catalyst layer via the following oxidation reaction:

$$CH_3OH + H_2O \rightarrow CO_2 + 6H^+ + 6e^- \quad (1)$$

Simultaneously gaseous oxygen reactant (O_2) passes through the porous gas diffusion layer and reaches the catalysis layer. The oxygen then reacts with electrons from the outer electric circuit and the protons passing across the membrane from the anode via the following reduction reaction:

$$6H_+ + 6e^- + 1.5O_2 \rightarrow 3H_2O \quad (2)$$

The passive vapor feed DMFC system in this study is a transient, multiphase and multi-component problem. Methanol and water are the only components considered in the liquid phase, while methanol, water, oxygen, carbon dioxide and nitrogen exist in the gas phase. The volume averaging for liquid and gaseous velocities for each individual phase within a control volume is applied to accommodate the fluid flow in the system [13]:

$$\langle \mathbf{V}_\ell \rangle^\ell = \frac{1}{V_\ell}\int_{V_\ell} \mathbf{V}_\ell \, dV, \quad \langle \mathbf{V}_g \rangle^g = \frac{1}{V_\ell}\int_{V_g} \mathbf{V}_g \, dV \quad (3)$$

Since the external vapor flow channel is at a different pressure and temperature than the fuel cell itself, a separate model is required which can describe the thermal management and the hydraulic behavior of the vapor feed DMFC system before the inlet conditions can be precisely specified. For the sake of mathematical modeling, the fuel cell system can be divided into two parts: porous regions and flow channel. The porous regions include the backing and catalyst layers of two electrodes and a membrane separator. The multi-fluid model [13] is applied for all the porous regions in the vapor feed DMFC, while the hydrodynamic model controlled by methanol/water condensation and evaporation is utilized in the anode flow channel. The simulation of porous regions is based on the solutions of the governing equations in the liquid and gas phases including continuity equations, momentum equations, species equations, energy equations and electrochemical equations (potential equations), which are described as follows.

2.1. Continuity equations

The continuity equations for the liquid and gas phase, in terms of liquid saturation, s, and the volume-averaged velocities are

$$\frac{\partial}{\partial t}(\varepsilon s \rho_l) + \nabla \cdot (\varepsilon s \rho_l \langle \mathbf{V}_l \rangle^l) = \sum_i \dot{m}'''_{R,l,i} + \sum_i \dot{m}'''_{T,gl,i} \quad (4)$$

$$\frac{\partial}{\partial t}(\varepsilon (1-s) \rho_g) + \nabla \cdot (\varepsilon (1-s) \rho_g \langle \mathbf{V}_g \rangle^g) = \sum_i \dot{m}'''_{R,g,i} - \sum_i \dot{m}'''_{T,gl,i} \quad (5)$$

where the mass generation terms are a sum of the reaction rates (subscript R) and the mass transfer rates from the gas to the liquid phase (subscript T) of each component.

2.2. Momentum equations

Taken into account the two forces acting in the fluid: drag caused by ion movement under electric field (electro-osmotic effect) and pressure gradient (Poiseuille flow in the pores), the convective flow velocities in porous regions can be written in Darcy's formation:

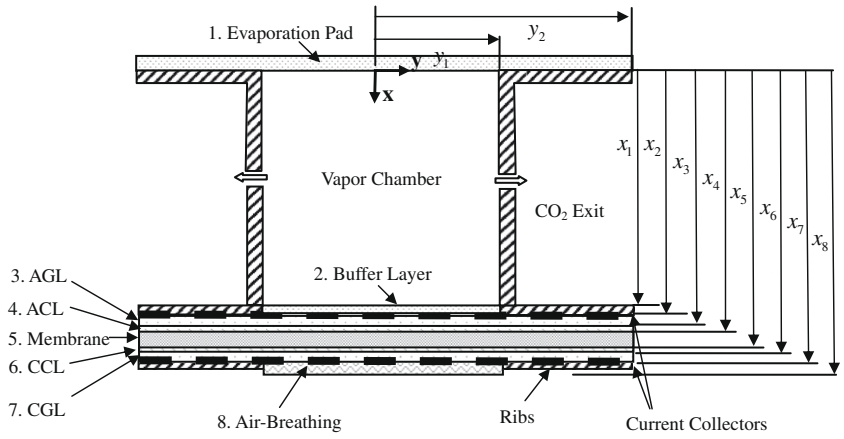

Fig. 1. Schematic diagram of a cross-section of a vapor feed DMFC system.

$$\varepsilon s\langle \mathbf{V}_l\rangle^l = -\frac{k_{rl}\mathbf{K}}{\mu_l}(\nabla p_l - \rho_l \mathbf{g}) + \frac{n_d M_l}{\rho_l}\frac{\mathbf{I}_p}{F} \tag{6}$$

$$\varepsilon(1-s)\langle \mathbf{V}_g\rangle^g = -\frac{k_{rg}\mathbf{K}}{\mu_g}(\nabla p_g - \rho_g \mathbf{g}) \tag{7}$$

The first term on the right-hand side of Eq. (6) and (7) represents the driven force of the fluid velocity caused by pressure gradient and gravity. The second term in Eq. (6) is the electro-osmotic drag in the membrane of the DMFC. The increase in viscous resistance due to each void being partially filled with a particular phase is defined as relative permeability [14].

$$k_{rl} = s^3 \quad \text{and} \quad k_{rg} = (1-s)^3 \tag{8}$$

The capillary pressure depends on the interfacial tension between liquid and vapor phases in the porous regions, which can be described by the cubic Leverette function [15]:

$$p_c = p_g - p_l = \sigma\cos\theta\left(\frac{\varepsilon}{K}\right)^{1/2} J(s) \tag{9}$$

$$J(s) = \begin{cases} 1.417(1-s) - 2.120(1-s)^2 + 1.263(1-s)^3, & \theta < \pi/2.0 \\ 1.417s - 2.120s^2 + 1.263s^3, & \theta \geqslant \pi/2.0 \end{cases} \tag{10}$$

2.3. Species equations

The species equations in liquid and gas in the porous regions are

$$\frac{\partial}{\partial t}(\varepsilon s\rho_l\omega_{l,i}) + \nabla\cdot(\dot{\mathbf{m}}''_{l,i}) = \dot{m}'''_{l,i} \tag{11}$$

$$\frac{\partial}{\partial t}(\varepsilon(1-s)\rho_g\omega_{g,i}) + \nabla\cdot(\dot{\mathbf{m}}''_{g,i}) = \dot{m}'''_{g,i} \tag{12}$$

The total mass flux (the sum of the advection and diffusion fluxes) of each species is represented by $\dot{\mathbf{m}}_{l,i}$ and $\dot{\mathbf{m}}_{g,i}$, in the liquid and gas phase, respectively.

$$\dot{\mathbf{m}}''_{l,i} = \varepsilon s\rho_l\langle \mathbf{V}_l\rangle^l\omega_{l,i} - [\varepsilon s]^\tau\rho_l D_{l,12}\nabla\omega_{l,i} \tag{13}$$

$$\dot{\mathbf{m}}''_{g,i} = \varepsilon(1-s)\rho_g\langle \mathbf{V}_g\rangle^g\omega_{g,i} - \sum_{j=1}^{N-1}[\varepsilon(1-s)]^\tau\rho_g D_{eff,ij}\nabla\omega_{g,j} \tag{14}$$

The diffusion of ideal gases in a multi-component mixture is expressed by a Stefan–Maxwell [13] equation after some mathematical manipulation.

$$[D_{eff,ij}] = \mathbf{A}^{-1}\mathbf{B} \tag{15}$$

$$A_{ii} = -\frac{\omega_{g,i}M_g^2}{D_{iN}M_N M_i} - \sum_{\substack{k=1\\k\neq i}}^{N}\frac{\omega_{g,k}M_g^2}{D_{ik}M_k M_i},$$
$$A_{ij} = \omega_{g,i}\frac{M_g^2}{M_i}\left(\frac{1}{D_{ij}M_j} - \frac{1}{D_{iN}M_N}\right), \quad i\neq j \tag{16}$$

$$B_{ii} = -\frac{M_g}{M_i}\left(1 - \frac{M_g\omega_{g,i}}{M_i}\right) - \frac{M_g^2\omega_{g,i}}{M_i M_N},$$
$$B_{ij} = \frac{M_g^2\omega_{g,i}}{M_i}\left(\frac{1}{M_j} - \frac{1}{M_N}\right), \quad i\neq j \tag{17}$$

For the condensable gases, the liquid and vapor phases are considered to be in thermal dynamic equilibrium. Equilibrium is found using Raoult's law, where the saturation pressure is calculated by the Clausius–Clapeyron equation.

$$\omega_{g,i} = \beta_i\omega_{l,i}$$
$$\beta_i = \frac{M_l p_{ref}}{M_g p_{op}}\exp\left(\frac{h_{fg}M_i}{R}\left(\frac{1}{T_{ref}} - \frac{1}{T}\right)\right) \tag{18}$$

2.4. Energy equations

A thermal balance is done in order to obtain the energy equation, taking into account the energy produced in the chemical reaction and phase change, the energy supplied in the form of electricity. The energy equation used in the porous regions of the DMFC is written as

$$\frac{\partial}{\partial t}(\varepsilon s\rho_l h_l + \varepsilon(1-s)\rho_g h_g + (1-\varepsilon)h_s) + \sum_i \nabla\cdot(\dot{\mathbf{m}}''_{l,i}h_{l,i} + \dot{\mathbf{m}}''_{g,i}h_{g,i})$$
$$= \nabla\cdot(k_{eff}\nabla T) + \nabla\cdot(\phi_m\sigma_m\nabla\phi_m) + \nabla\cdot(\phi_c\sigma_c\nabla\phi_c) \tag{19}$$

In the present simulations, the specific heat is considered to be constant. The enthalpy can be written as sensible heat, $\bar{h}$, plus the heat of formation, h^0. Taking the species mass balance into consideration, the energy equation can be rewritten in terms of the sensible heat transport and the heat generation terms that coincide with the reaction rates and phase change.

$$\frac{\partial}{\partial t}(\varepsilon s\rho_l\bar{h}_l + \varepsilon(1-s)\rho_g\bar{h}_g + (1-\varepsilon)\bar{h}_s) + \sum_i \nabla\cdot(\dot{\mathbf{m}}''_{l,i}\bar{h}_{l,i} + \dot{\mathbf{m}}''_{g,i}\bar{h}_{g,i})$$
$$= \nabla\cdot(k_{eff}\nabla T) - \sum_i \dot{m}'''_{l,i}h^0_{l,i} - \sum_i \dot{m}'''_{g,i}h^0_{g,i} + \nabla\cdot(\phi_m\sigma_m\nabla\phi_m)$$
$$+ \nabla\cdot(\phi_c\sigma_c\nabla\phi_c) \tag{20}$$

The total sensible enthalpy in each phase is based on mass weighted averaging:

$$\bar{h}_l = \sum_i \omega_{l,i}\bar{h}_{l,i} \tag{21}$$

$$\bar{h}_g = \sum_i \omega_{g,i}\bar{h}_{g,i} \tag{22}$$

The effective thermal conductivity is

$$k_{eff} = \varepsilon s k_l + \varepsilon(1-s)k_g + (1-\varepsilon)k_s \tag{23}$$

2.5. Potential equations

The electrochemical reactions of methanol oxidation at the anode and oxygen reduction at the cathode are both complicated multistage processes, which can be divided into the electric potential of the carbon phase and the membrane phases. The two types of potential govern the motion of protons and that of electrons, respectively. Taking local electro-neutrality into account, the electronic current and ionic current produced or consumed in the catalyst layers lead to a voltage drop via Ohm's law according to the following governing equations:

$$\nabla\cdot(\sigma_c\nabla\phi_c) - R_{ox} + R_{red} = 0 \tag{24}$$

$$\nabla\cdot(\sigma_m\nabla\phi_m) + R_{ox} - R_{red} = 0 \tag{25}$$

The oxidation and reduction reaction rates are R_{ox} and R_{red}, respectively. The reaction rates are modeled from the expression developed by Meyers and Newman [16].

$$R_{ox} = a_{ox}I^{MeOH}_{0,ref}\frac{c_{MeOH}}{c_{MeOH} + \lambda\exp(\alpha_a\eta_a\frac{F}{R_uT})}\exp\left(\alpha_a\eta_a\frac{F}{R_uT}\right) \tag{26}$$

$$R_{red} = a_{red}I^{O_2}_{0,ref}\frac{\omega_{O_2}}{\omega_{O_2,ref}}\exp\left(\alpha_c\eta_c\frac{F}{R_uT}\right) \tag{27}$$

where the overpotentials at the anode and the cathode are defined by

$$\eta_a = \phi_c - \phi_m - U^{MeOH} \tag{28}$$

$$\eta_c = U^{O_2} + \phi_m - \phi_c \tag{29}$$

Once the values of the overpotentials at the anode and the cathode are calculated, the cell voltage can be determined as follows:

$$V_{cell} = U^{O_2} - U^{MeOH} - \eta_a - \eta_c - \frac{I_{cross}\delta_m}{\sigma_m} \tag{30}$$

The reaction rates for the species equations are

$$\dot{m}'''_{R,l,MeOH} = -\frac{R_{ox}}{6F}M_{MeOH}, \quad \dot{m}'''_{R,l,H_2O} = \left(-\frac{R_{ox}}{6F} + \frac{R_{red}}{2F}\right)M_{H_2O} \tag{31}$$

$$\dot{m}'''_{R,g,CO_2} = \frac{R_{ox}}{6F}M_{CO_2}, \quad \dot{m}'''_{R,g,O_2} = -\frac{R_{red}}{4F}M_{O_2} \tag{32}$$

2.6. Anode flow channel

In the anode flow channel, local thermodynamics equilibrium prevails at the interfaces of the flow channel, the gas phase in the anode flow channel can be considered saturated with water and methanol vapors. In order to describe the evaporation and condensation dynamics at the flow channel/evaporation pad and flow channel/buffer layer interfaces, the equations proposed in [18] is applied to describe the mass balance in the flow channel:

$$\frac{dm_{MeOH}}{dt} = A_{fc}(P_{sat,MeOH}(T_{fc}) - P_{MeOH})\sqrt{\frac{M_{MeOH}}{2\pi RT_{fc}}} \tag{33}$$

$$\frac{dm_{H_2O}}{dt} = A_{fc}(P_{sat,H_2O}(T_{fc}) - P_{H_2O})\sqrt{\frac{M_{H_2O}}{2\pi RT_{fc}}} + \frac{h_m\rho_g(w_{g,H_2O,buff} - w_{g,H_2O,fc})}{\delta_{fc}} \tag{34}$$

The $\dot{m}_{evap}$ value is positive when the methanol/water partial pressure is smaller than the saturation pressure, causing the methanol/water to evaporate in that case. When the methanol/water condenses, the value is negative. Methanol/water vapor partial pressures inside the anode flow channel are defined as

$$P_{MeOH} = \frac{RT_{fc}m_{MeOH}}{M_{MeOH}V_{fc}} \quad \text{and} \quad P_{H_2O} = \frac{RT_{fc}m_{H_2O}}{M_{H_2O}V_{fc}} \tag{35}$$

The energy equation at the anode flow channel can be written as

$$\rho c_p V_{fc}\frac{dT_{fc}}{dt} = \dot{q}_{electric} - h_{\ell v,MeOH}\dot{m}_{MeOH} - h_{\ell v,H_2O}\dot{m}_{H_2O} + hA_{fc}(T_{s,buffer} - T_{fc}) \tag{36}$$

The heat and mass transfer coefficient is taken from the natural convection correlations on a horizontal surface facing up.

$$h = Nu\frac{k}{L}, \quad Nu = 0.54(Gr\mathrm{Pr})^{.025}, \quad Gr = \frac{g\rho|\Delta\rho|L^3}{\mu^2}$$
$$h_m = Sh\frac{\rho D_{ij}}{L}, \quad Sh = 0.54(GrSc)^{.025} \tag{37}$$

The heat and mass transfer coefficients at the surface of the air-breathing layer are taken as a horizontal surface facing down.

$$h = Nu\frac{k}{L}, \quad Nu = 0.27(Gr\mathrm{Pr})^{.025}$$
$$h_m = Sh\frac{\rho D_{ij}}{L}, \quad Sh = 0.27(GrSc)^{.025} \tag{38}$$

2.7. Solution procedure

Table 1 contains the initial and boundary conditions used in the vapor feed passive DMFC model. The governing equations for momentum, species, energy and potentials are discretized and solved in a coupled manner by the finite volume method. The flow variables are solved by a Gauss-Siedel iteration scheme. The first-order upwind scheme is utilized for the convection terms in all the conservation equations, including momentum and species equations. The whole solution procedure for the governing equations is as follows:

Table 1
Physicochemical and kinetic parameters in the numerical modeling.

Parameter/symbol	Value	Ref.
Volume of the flow channel/V_{fc}	1.8×10^{-5} m^3	
Cross-sectional area of the flow channel/A_{fc}	9×10^{-4} m^2	
Height of the flow channel/	2×10^{-2} m	
Thickness/Porosity/Tortuosity/Permeability of AGL and CGL	1.5×10^{-4} m/0.7/1.1/4×10^{-11}	
Thickness/Porosity/Tortuosity/Permeability of ACL and CCL	2.3×10^{-5} m/0.6/1.3/5×10^{-11}	
Thickness/Porosity/Tortuosity/Permeability of membrane	1.8×10^{-4} m/0.5/1.8/1×10^{-12}	
Thickness/Porosity/Tortuosity/Permeability of air-breathing	2.54×10^{-4} m/0.2/1.1/7.24×10^{-13}	
Gas diffusivity of O_2,CO_2/O_2,H_2O/O_2,N_2/CO_2,H_2O/CO_2,N_2/H_2O,N_2	1.59×10^{-5}/2.44×10^{-5}/2.02×10^{-5}/1.62×10^{-5}/1.6×10^{-5}/2.42×10^{-5}	Lide[19]
Viscosity of liquid methanol/water	4.46×10^{-4}/6.513×10^{-4}	Faghri and Zhang [13]
Viscosity of gas/μ_g	2.03×10^{-5}	Wang and Wang [15]
Density of liquid water/ρ_{ℓ,H_2O}	$\exp\left(6.9094 - 2.0146\times10^{-5}(T-273) - 5.9868\times10^{-6}(T-273)^2 + 2.5921\times10^{-8}(T-273)^3 - 9.3244\times10^{-11}(T-273)^4 + 2.5921\times10^{-13}(T-273)^5\right)$	Faghri and Zhang [13]
Density of liquid methanol/$\rho_{\ell,MeOH}$	$244.4\times0.224^{[1(1-T/513)^{2/7}]}$	Yaws [20]
Liquid diffusivity of water and methanol	$10^{-5.4163-999.78/T}$ m^2/s	
Electro-osmotic drag coefficient of water/$n_d^{H_2O}$	$2.9\exp[1029(1/333 - 1/T)]$	Guo and Ma [21]
Electro-osmotic drag coefficient of methanol/n_d^{MeOH}	$n_d^{H_2O}x^{MeOH}$	Ren et al. [22]
Electric conductivity of carbon/membrane phase/σ_c,σ_m	4000/3.4	Rice and Faghri [17]
Specific reaction area at the electrodes/a_{ox},a_{red}	43,478	
Transfer coefficient at anode and cathode/α_a,α_c	0.35/0.79	Assumed
Reference exchange current density on anode/$I_{0,ref}^{MeOH}$	$94.25\exp(35570/R(1/353 - 1/T))$	Wang and Wang [15]
Reference exchange current density on cathode, $I_{0,ref}^{O_2}$	$0.04222\exp(77200/R(1/353 - 1/T))$	
Thermodynamic potential of oxygen reduction/$U_0^{O_2}$	1.24 V	Rice and Faghri [17]
Thermodynamic potential of methanol oxidation/U_0^{MeOH}	−0.0229 V	

1. Assume the cell voltage, solve electric potentials, and update reaction kinetics.
2. Solve for saturation and liquid/gas pressure.
3. Solve species equations and energy equation.
4. Calculate the temperature and condensation/evaporation rate at the flow channel.
5. Obtain the methanol concentration at the surface of the buffer layer and the cell voltage, treat them as the new guessed ones and update the properties.
6. Go back to step 1 and repeat until converged, then go to next time step.

The physicochemical properties, operation conditions and boundary conditions for the simulation of a vapor feed DMFC system are illustrated in Table 1–3. The calculation domain for the DMFC simulation is divided into 170×50 elements. A sensitivity analysis was conducted by doubling the number of elements in the mesh for the case without heating. The deviation of the results on average was less than 2.0% and so is assumed to be meshing independent. The solutions are considered to be convergent when the relative error between two consecutive iterations in each field was less then 10^{-5}.

3. Results and discussion

The complexity of the model requires special experiments for the verification of its merits. Fig. 2 shows the good agreement between the numerical results and experimental data under the same operation condition. Fig. 2(A) compares the experimental data with the numerical calculation for the transient voltage outputs against the experimental data under different electric power with a constant current density of 50 mA/cm^2. The operation temperature is set to be 30 °C and the relative humidity is 50%. As can be seen, the voltage decreases sharply at the beginning and then slows down afterwards. For the case without electric heating, since the evaporation rate of the fuel cell is low, the voltage decreases sharply because of the mass limitation during the stage between 4 and 7 h. Longer cell performance is achieved with higher electric power because the evaporation rate of the methanol at the evaporation pad as well as the methanol concentration at the anode inlet increases under higher electric power. Fig. 2(B) compares the experimentally obtained cell polarization data with their numerical modeling. Because the evaporation rate of fuel and the methanol concentration at the anode inlet increase with the increasing electric power, results in the increasing methanol crossover through the membrane, the cell voltage decreases when the electro power increases. The cell power density, i.e., the product of cell voltage and the current density, also decreases with the increasing electro power.

Fig. 3 shows the variation of methanol concentration at the anode inlet under the same condition of Fig. 2. As can be seen, the methanol fraction increases rapidly at the beginning due to the high saturate pressure gradient at the surfaces of the evaporation pad driving the transport of water and methanol. The methanol fraction drops slowly after the methanol consumption and the generated water prevails against the methanol input at the flow channel. On the other hand, the increasing rate of the methanol fraction at the beginning is more rapid with the increasing electric power as the higher fuel cell temperature caused by the electrochemical reaction accelerates the methanol evaporation of the evaporative pad. Fig. 4 shows the variation of cell temperature at the anode inlet under the same condition of Fig. 2. It is found that the transient cell temperature varied with a trend similar to the transient methanol fraction shown in Fig. 3. This behavior indicates that the input methanol fraction can be attributed to the differences in the temperature variation. It should also be noted that the temperature decreases at the beginning for the cases without electric heating or lower heating. This is mainly due to the absorption of latent heat for the evaporation of methanol as illustrated in Eq. (32).

Since overpotential represents voltage which is sacrificed to overcome the activation barrier associated with the electrochemical reaction, it is necessary to illustrate the reaction characteristic by overpotentials at the electrodes. Fig. 5 shows the average overpotentials at the anode and cathode under the same condition of Fig. 2. The anodic overpotential increases smoothly at the beginning and then increases rapidly when it reaches the mass limit. When the electric power increases, the anodic overpotential is lowered due to the increasing methanol crossover. For the cathodic overpotential, it increases at the beginning and then decreases at a relatively lower rate. The cathodic overpotential increases when the electric power increases.

Fig. 6 shows the electric power effect on the methanol crossover through the membrane under the same condition of the Fig. 2. The methanol crossover increases at the beginning because the methanol condensation at the inlet of the fuel cell is dominant at the beginning and then decreases when the consumption rate is faster than the condensation input. Since the increasing electric power increases the cell operating temperature and the feed methanol concentration at the anode inlet, the methanol crossover increases with the increase of the electric power.

Fig. 7 shows the polarization effect on the mass fraction of methanol at the anode inlet under the same condition of the Fig. 2. The mass fraction decreases quickly at the low current densities and then becomes smooth in the high current densities. The maximum methanol fraction and the decreasing rate increase with

Table 2
Operation conditions.

Parameter	Value
Operating temperature	30 °C
Anode flow channel pressure	0.02 psi
Cathode pressure	1 atm
Inlet liquid saturation at anode	100%
Inlet liquid saturation at cathode	0% (fully humidified air)
Cell operating current density	50 mA/cm^2
Methanol content in the evaporation pad	1 g
Water content in the buffer layer	1 g

Table 3
Boundary conditions in the porous regions.

Governing equation	$x = x_1$	$x = x_1$	$x = x_3$	$x = x_{acl}$	$x = x_m$	$x = x_{ccl}$	$x = x_{cgdl}$
Momentum	$p_g = p_{fc}$	–	–	–	–	–	$p_g = p_{ca}$
	$\nabla p_\ell = 0$	–	–	–	–	–	$\nabla p_\ell \cdot \mathbf{n} = 0$
Gas transport	$\nabla \omega_{g,i} = 0$	–	–	–	–	–	$-[\varepsilon(1-s)]^\tau \nabla \omega_{g,i} \cdot \mathbf{n} = h_m(\omega_{g,i} - \omega_{g,i,\infty})$
Liquid transport	$\dot{\mathbf{m}}''_{l,i} = h_m\left(\frac{\omega_{fc,i}}{-\omega_{buff,i}}\right)$	–	–	–	–	–	$\nabla \omega_{\ell,i} \cdot \mathbf{n} = 0$
Membrane potential	–	–	$\nabla \varphi_m \cdot \mathbf{n} = 0$	–	–	$\nabla \varphi_m \cdot \mathbf{n} = 0$	–
Catalyst potential	–	$-\sigma_c \frac{\partial \phi_c}{\partial x} = I_{cell}$	–	$\nabla \varphi_c \cdot \mathbf{n} = 0$	$\nabla \varphi_c \cdot \mathbf{n} = 0$	–	$\varphi_c = V_{cell}$
Energy	$-k_{eff} \nabla T \cdot \mathbf{n} = h(T - T_{fc})$	–	–	–	–	–	$-k_{eff} \nabla T \cdot \mathbf{n} = h(T - T_\infty)$

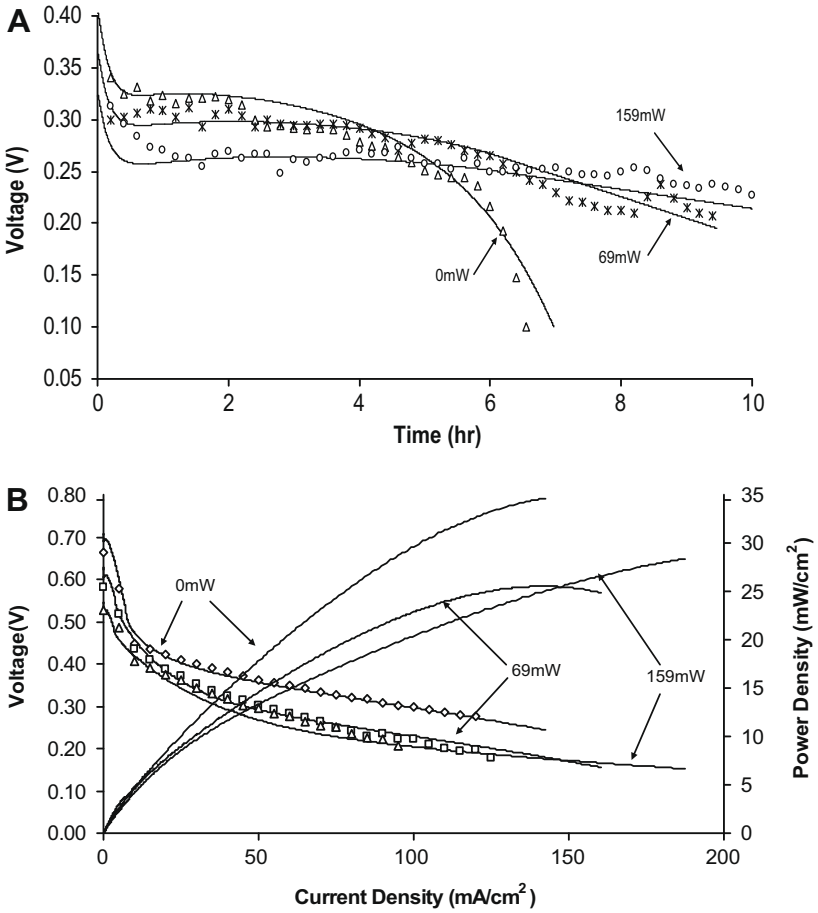

Fig. 2. Validation of the present DMFC model against the experimental data at different electric power with an operation temperature of 30 °C and a current density of 50 mA/cm^2. (A) Transient voltage outputs; (B) polarization curves.

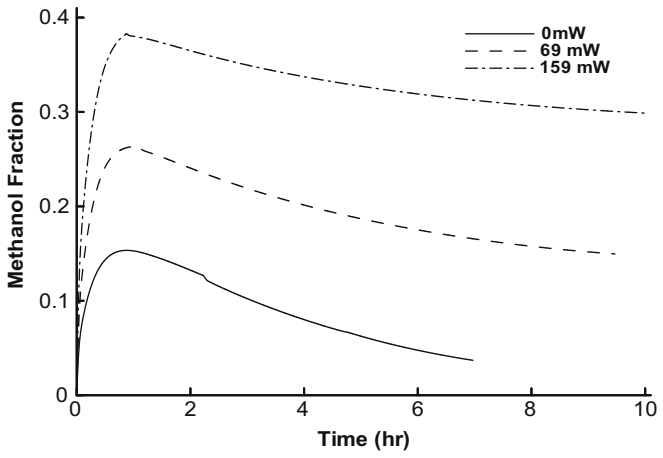

Fig. 3. Variation of methanol fraction at the anode inlet under different electric power with an operation temperature of 30 °C and a current density of 50 mA/cm^2.

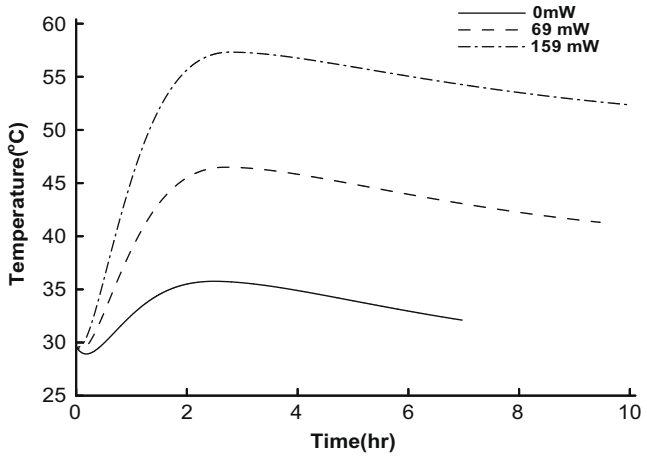

Fig. 4. Variation of the temperature at the anode inlet under different electric power with an operation temperature of 30 °C and a current density of 50 mA/cm^2.

the increasing electric heating. Fig. 8 shows the polarization effect on temperature at the anode inlet under the same condition of the Fig. 2. Temperature increases to the maximum at a low density and then decreases afterward. The decreasing rate slows down with the increasing current density. The maximum temperature and the decreasing rate increase as the electric heating increases. Fig. 9 shows the polarization effect on the anodic and cathodic overpotentials under the same condition of the Fig. 2. The anodic overpotential increase rapidly at the beginning and then the increasing rate slows down with the increasing current density. The anodic overpotential increases when the electric power increases. The cathodic overpotential decreases rapidly at the beginning and then the decreasing rate slows down with the increasing current density. The cathodic overpotential decreases when the electric power increases. Fig. 10 shows the polarization effect on the methanol crossover under the same condition of the Fig. 2. Methanol

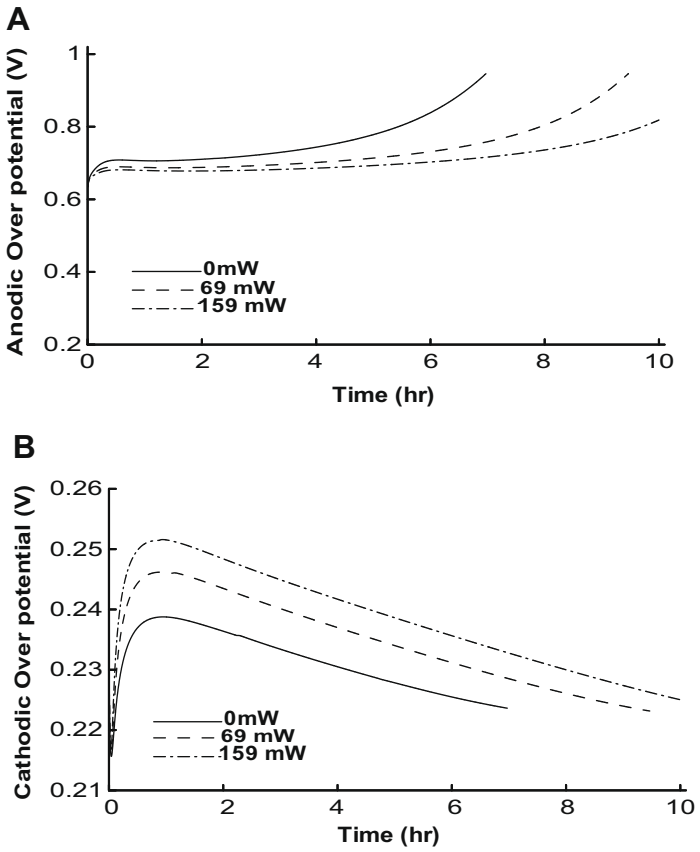

Fig. 5. Variation of electrode overpotentials under different electric power with an operation temperature of 30 °C and a current density of 50 mA/cm^2.

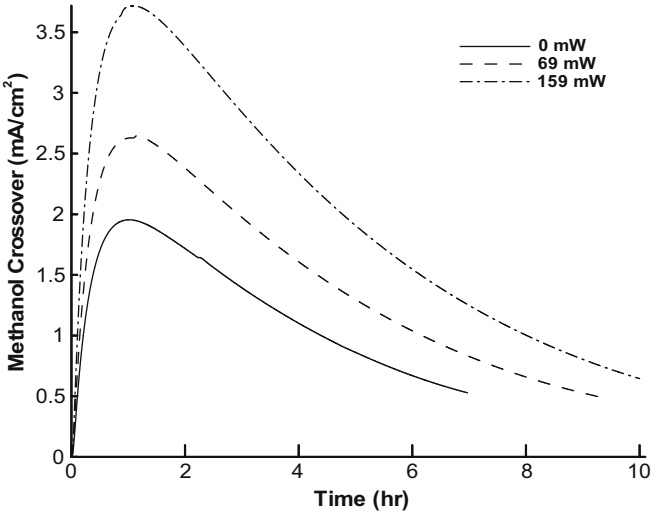

Fig. 6. Variation of methanol crossover under different electric power with an operation temperature of 30 °C and a current density of 50 mA/cm^2.

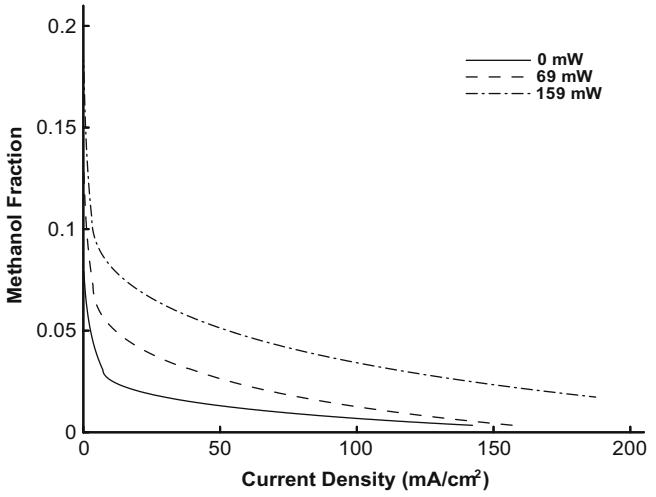

Fig. 7. Methanol fraction at the anode inlet as a function of cell current density under different electric power with an operation temperature of 30 °C and a current density of 50 mA/cm^2.

crossover decreases quickly at the beginning and then the decreasing rate slows down with the increasing current density. The maximum methanol crossover increases and the decreasing rate decreases when the electric power increases.

4. Conclusion

In this paper, a two-dimensional, multiphase model was developed, considering the coupled multi-component transport processes as well as electrochemical phenomena in the membrane and electrodes in a vapor feed DMFC system. Conservation equations of mass, momentum, species transport, and the potential with electrochemical reaction are numerically solved in the coupled manner. The numerical calculations are compared with the experimental data in a good agreement. The transient and polarization characteristics of the DMFC are intensively discussed. The results not only reveal the information such as the evolution of voltage output, methanol fraction, temperature, overpotentials

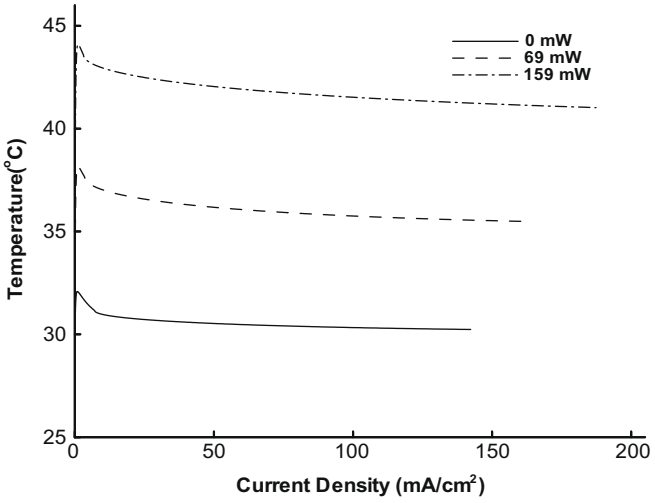

Fig. 8. Temperature at the anode inlet as a function of cell current density under different electric power with an operation temperature of 30 °C and a current density of 50 mA/cm^2.

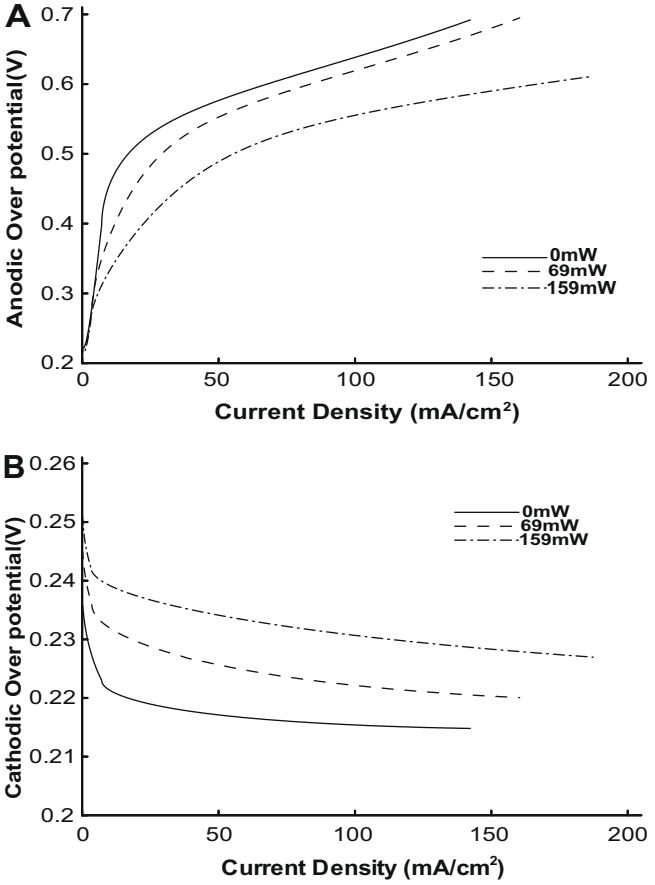

Fig. 9. Electrode overpotentials as a function of cell current density under different electric power with an operation temperature of 30 °C and a current density of 50 mA/cm^2.

and methanol crossover through the membrane, but also suggest a key parameter, the anode flow channel, to achieve optimized cell performance.

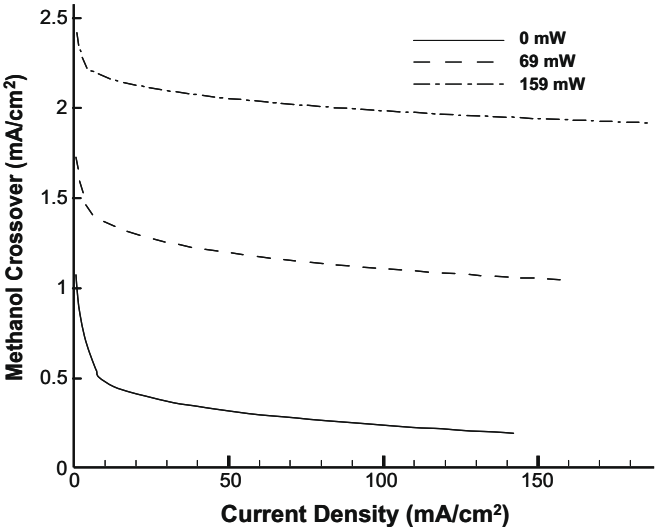

Fig. 10. Methanol crossover as a function of cell current density under different electric power with an operation temperature of 30 °C and a current density of 50 mA/cm^2.

References

[1] T.J. Yen, N. Fang, X. Zhang, A micro methanol fuel cell operating at near room temperature, Appl. Phys. Lett. 83 (2003) 4056–4058.
[2] G.Q. Lu, C.Y. Wang, Development of high performance micro DMFCS and a DMFC stack, J. Fuel Cell Sci. Tech. 3 (2006) 31–136.
[3] J.G. Liu, T.S. Zhao, R. Chen, C.W. Wong, The effect of methanol concentration on the performance of a passive DMFC, Electrochem. Commun. 7 (2005) 288–294.
[4] K. Scott, W. Taama, J. Cruickshank, Performance and modeling of a direct methanol solid polymer electrolyte fuel cell, J. Power Sources 65 (1997) 159–171.
[5] J. Cruickshank, K. Scott, The degree and effect of methanol crossover in the direct methanol fuel cell, J. Power Sources 70 (1998) 40–47.
[6] K. Scott, W.M. Taama, P. Argyropoulos, Engineering aspects of the direct methanol fuel cell system, J. Power Sources 79 (2001) 43–59.
[7] H. Kim, Passive direct methanol fuel cells fed with methanol vapor, J. Power Sources 162 (2006) 1232–1235.
[8] Z. Guo, A. Faghri, Vapor feed direct methanol fuel cells with passive thermal-fluids management system, J. Power Sources 167 (2007) 378–390.
[9] G. Jewett, Z. Guo, A. Faghri, Performance characteristics of a vapor feed passive miniature direct methanol fuel cell, Int. J. Heat Mass Transfer, submitted.
[10] H. Dohle, J. Divisek, R. Jung, Process engineering of the direct methanol fuel cell, J. Power Sources 86 (1-2) (2000) 469–477.
[11] A.A. Kulikovsky, J. Divisek, A.A. Kornyshev, Two-dimensional simulation of direct methanol fuel cell: a new (embedded) type of current collector, J. Electrochem. Soc. 147 (3) (2000) 952–959.
[12] J. Rice, A. Faghri, Analysis of a passive vapor feed direct methanol fuel cell, Int. J. Heat Mass Transfer 51 (2008) 948–959.
[13] A. Faghri, Y. Zhang, Transport Phenomena in Multiphase Systems, Elsevier, Amsterdam, 2006.
[14] M. Kaviany, Principles of Heat Transfer in Porous Media, 2nd ed., Springer, Berlin, 1999.
[15] Z.H. Wang, C.Y. Wang, Mathematical modeling of liquid-feed direct methanol fuel cells, J. Electrochem. Soc. 150 (4) (2003) A508–A519.
[16] J.P. Meyers, J. Newman, Simulation of the direct methanol fuel cell, J. Electrochem. Soc. 149 (6) (2002) A718–A728.
[17] J. Rice, A. Faghri, Thermal and start-up characteristics of a miniature passive liquid feed DMFC system, including continuous /discontinuous phase limitations, ASME J. Heat Transfer 130 (2006).
[18] M.W. Zemansky, R.H. Dittman, Heat Thermodynamics, McGraw-Hill, New York, 1981.
[19] D.R. Lide (Ed.), Handbook of Chemistry and Physics, eighty fifth ed., CRC Press, USA, 2004.
[20] C.L. Yaws, Thermodynamic and Physical Property Data, Gulf Pub. Co., Houston, TX, 1990.
[21] H. Guo, C.F. Ma, 2D analytical model of a direct methanol fuel cell, Electrochem. Commun. 6 (2004) 306–312.
[22] X. Ren, T.E. Springer, A. Zawodzinski, S. Gottesfeld, Methanol transport through nafion membranes, electro-osmotic drag effects on potential step measurements, J. Electrochem. Soc. 147 (2) (2000) 466–474.